



Rapid age assessment of glacial landforms in the Pyrenees using Schmidt Hammer exposure dating (SHED)

DOI:
[10.1017/qua.2018.12](https://doi.org/10.1017/qua.2018.12)

Document Version
Accepted author manuscript

[Link to publication record in Manchester Research Explorer](#)

Citation for published version (APA):

Tomkins, M., Dortch, J., Hughes, P., Huck, J., Stimson, A., Delmas, M., Calvet, M., & Pallas, R. (2018). Rapid age assessment of glacial landforms in the Pyrenees using Schmidt Hammer exposure dating (SHED). *Quaternary Research*, 90(1), 26-37. <https://doi.org/10.1017/qua.2018.12>

Published in:
Quaternary Research

Citing this paper

Please note that where the full-text provided on Manchester Research Explorer is the Author Accepted Manuscript or Proof version this may differ from the final Published version. If citing, it is advised that you check and use the publisher's definitive version.

General rights

Copyright and moral rights for the publications made accessible in the Research Explorer are retained by the authors and/or other copyright owners and it is a condition of accessing publications that users recognise and abide by the legal requirements associated with these rights.

Takedown policy

If you believe that this document breaches copyright please refer to the University of Manchester's Takedown Procedures [<http://man.ac.uk/04Y6Bo>] or contact uml.scholarlycommunications@manchester.ac.uk providing relevant details, so we can investigate your claim.



1 Rapid age assessment of glacial landforms in the
2 Pyrenees using Schmidt Hammer exposure dating
3 (SHED)

4 **Matt D. Tomkins¹, Jason M. Dortch^{1,2}, Philip D. Hughes¹, Jonny J.**
5 **Huck¹, Andrew Stimson¹, Magali Delmas³, Marc Calvet³, and Raimon**
6 **Pallàs⁴**

7 *¹Cryosphere Research at Manchester, Department of Geography, University of Manchester, Manchester,*
8 *M13 9PL, United Kingdom*

9 *²Kentucky Geological Survey, 228 Mining and Mineral Resources Building, University of Kentucky, Lexington,*
10 *KY 40506, United States of America*

11 *³UMR CNRS 7194 HNHP, Université de Perpignan Via Domitia, Perpignan, France*

12 *⁴Departament de Dinàmica de la Terra i de l'Oceà, Universitat de Barcelona, 08028 Barcelona, Spain*

13

14

15

16

17

18

19

20

21

22 **ABSTRACT**

23 Schmidt Hammer (SH) sampling of 54 ^{10}Be dated granite surfaces from the Pyrenees reveals a clear
24 relationship between exposure and weathering through time ($n = 52$, $R^2 = 0.96$, $p < 0.01$) and
25 permits the use of the SH as a numerical dating tool. To test this ^{10}Be -SH calibration curve, 100
26 surfaces were sampled from 5 ice-front positions in the Têt catchment, Eastern Pyrenees, with
27 results verified against independent ^{10}Be and ^{14}C ages. Gaussian modelling differentiates Holocene
28 (9.4 ± 0.6 ka), Younger Dryas (12.6 ± 0.9 ka), Oldest Dryas (16.1 ± 0.5 ka), Last Glacial Maximum
29 (LGM: 24.8 ± 0.9 ka) and Würmian Maximum Ice Extent stages (MIE: 40.9 ± 1.1 ka). These data
30 confirm comparable glacier lengths during the LGM and MIE (~ 300 m difference), in contrast to
31 evidence from the Western Pyrenees (≥ 15 km), reflecting the relative influence of Atlantic and
32 Mediterranean climates. Moreover, Pyrenean glaciers advanced significantly during the LGM, with a
33 local maximum at ~ 25 ka, driven by growth of the Laurentide Ice Sheet, southward advection of the
34 polar front and a solar radiation minimum in the Northern Hemisphere. This calibration curve is
35 available at <http://shed.earth> to enable wider application of this method throughout the Pyrenees.

36

37 **INTRODUCTION**

38 The Quaternary glacial record of the Pyrenees is essential for reconstructing regional paleoclimate
39 and provides crucial information on the response of terrestrial ice masses to variability in the North
40 Atlantic atmosphere-ocean circulation system (Pallàs et al., 2010). However, determining causal links
41 between climate and glacier response is predicated on the development of robust chronological
42 frameworks. Recent advances in terrestrial cosmogenic nuclide (TCN) and optically stimulated
43 luminescence (OSL) dating techniques and their application to glacial and glacio-fluvial deposits have
44 helped constrain the chronology of Late Pleistocene glaciation (Würmian Stage) and in particular, the
45 timing of the Würmian Maximum Ice Extent (MIE). ^{10}Be ages from Ariège (Delmas et al., 2011; 2015)

46 and Malniu (Pallàs et al., 2010) show that MIE glaciers in the Eastern Pyrenees terminated just down-
47 valley of Last Glacial Maximum limits (LGM; 23.3 - 27.5 ka; Hughes and Gibbard, 2015). This appears
48 to contrast with glaciers in the Western Pyrenees, where LGM glaciers failed to reach MIE limits by
49 ~15 km (Jalut et al., 1992; Calvet et al., 2011; Delmas, 2015), perhaps reflecting the contrasting
50 influence of Atlantic and Mediterranean climates (Delmas et al., 2011). However, this hypothesis is
51 limited by the relative scarcity of geochronological data and the increasing fragmentation of trunk
52 glaciers into isolated ice masses during retreat and downwastage of the Pyrenean icefield. These
53 difficulties, exacerbated by the fragmentary nature of the geomorphological record, preclude
54 straightforward stratigraphic correlation of glacial deposits and have thus far prevented a Pyrenean-
55 scale synthesis of post-Marine Isotope Stage (MIS) 4 glaciation.

56 TCN dating is well suited to address this knowledge gap as glacial deposits are well preserved in the
57 Pyrenees. However, moraine stabilisation (Hallet and Putkonen, 1994) and nuclide inheritance
58 (Putkonen and Swanson, 2003) can result in 'young' and 'old' ages respectively (Heyman et al., 2011;
59 Murari et al., 2014). The most significant barrier to isolating these ages is the cost of TCN dating,
60 which often precludes high-sample studies and in turn, prevents statistically robust identification and
61 rejection of erroneous results. Thus, new cost and time-efficient dating techniques are necessary
62 which complement existing radiometric techniques and can be applied widely to undated glacial
63 landforms. In the British Isles, a clear relationship between TCN exposure ages and Schmidt
64 Hammer (SH) rebound values (R-values) was recorded for 54 dated granite surfaces ($R^2 = 0.94$, $p <$
65 0.01 ; 0.8 - 23.8 ka; Tomkins et al., 2016, 2018) and permits the estimation of exposure time based
66 on surface R-values. This TCN-SH calibration curve has been applied to glacial landforms in the
67 Mourne Mountains (Barr et al., 2017) and the Lake District (Tomkins et al., 2016), with results
68 consistent with existing radiometric ages (^{10}Be , ^{14}C). However, direct application of this calibration
69 curve to Pyrenean deposits is unsuitable as long-term weathering rates exhibit systematic variability
70 between climatic regimes (Riebe et al., 2004). This variability is likely significant between the
71 temperate-oceanic climate of the British Isles and the comparatively dry, continental Pyrenees. In
72 this paper, we develop and verify the first Pyrenean Schmidt Hammer exposure dating (SHED)

73 calibration curve and generate new chronological data to constrain the deglacial chronology of the
74 Têt glacier, a major outlet of the Pyrenean icefield. These new chronological data are supported by
75 independent ^{10}Be ages, are consistent with previous geomorphological assessments (Delmas et al.,
76 2008), and contribute significantly to our understanding of post-MIS 4 glacier dynamics.

77

78 **METHODS**

79 54 TCN dated granite surfaces were sampled using the N-Type Schmidt Hammer from across the
80 Pyrenees (Fig. 1; Table. 1; Pallàs et al., 2006, 2010; Crest et al., 2017). Sampled surfaces (Fig. 2)
81 include moraine boulders ($n = 39$) and ice-sculpted bedrock ($n = 15$) from a range of elevations (981
82 - 2817 m) and geomorphological settings. All surfaces were of sufficient size (Sumner and Nel, 2002)
83 and were free of surface discontinuities (Williams and Robinson, 1983) and lichen (Matthews and
84 Owen, 2008). Sampled surfaces were coarse to medium grained granite and granodiorite from the
85 Hercynian Axial Zone (Crest et al., 2017). Axial Zone granites were uplifted during and after the late
86 Cretaceous following collision of Europe and the Iberian microplate, with deformation ceasing at
87 $\sim 20\text{-}25$ Ma, followed by post-orogenic uplift over the last ~ 10 Ma (Gunnell et al., 2009; Ortuño et
88 al., 2013). The predominant style of weathering is sub-aerial, as evidenced by granular disintegration
89 of the crystalline rock surface (André, 2002). There is no clear variability in grain size or rock
90 composition between sites (Fig. 1B). 30 R-values were recorded per surface. This exceeds the
91 recommendation of Niedzielski et al. (2009) of 20 R-values for granite surfaces (Min. sample size in
92 terms of mean at $\alpha = 0.05$). Carborundum treatment was used to remove surface irregularities prior
93 to testing (Katz et al., 2000; Cerna & Engel, 2011; Engel et al., 2011; Viles et al., 2011; Kłapyta, 2013).
94 There is ongoing debate as to whether rock surfaces should be smoothed prior to testing (Moses et
95 al., 2014). However, the data presented in this study indicates that a consistent sampling approach
96 enables age-related information to be retained i.e. recently exposed surfaces (< 5 ka) generate
97 significantly different R-values from those exposed during the Younger Dryas, the LGM and the
98 Würmian MIE. R-values were recorded perpendicular to the tested surface to reduce the risk of

99 frictional sliding of the plunger tip (Viles et al., 2011), with single impacts separated by at least a
100 plunger width (Aydin, 2009) and no outliers were removed following Niedzielski et al. (2009).
101 Reported R-values are the arithmetic mean of 30 R-values and the standard error of the mean
102 (SEM). To account for Schmidt Hammer drift with use (Tomkins et al., 2018), instrument calibration
103 was based on the University of Manchester calibration boulder (Dortch et al., 2016) and performed
104 using SHED-Earth, an online calculator developed to enable wider and more consistent application of
105 SHED (Pre-data collection: 48.27 ± 2.02 ; Post-data collection: 48.23 ± 1.92 ; Correction Factor:
106 0.999).

107 ^{10}Be exposure ages were recalibrated using the online calculators formerly known as the CRONUS-
108 Earth online calculators (<http://hess.ess.washington.edu/math/>, Wrapper script 2.3, Main calculator
109 2.1, constants 2.3, muons 1.1; Balco et al., 2008). Exposure ages are based on the primary calibration
110 dataset of Borchers et al. (2016), the time-dependent L_m scaling (Lal, 1991; Stone, 2000) and
111 assuming 0 mm ka^{-1} erosion. This approach is suitable as erosion rates for most glaciated crystalline
112 rock surfaces are usually low ($0.1 - 0.3 \text{ mm ka}^{-1}$; André, 2002). Recalibrated ages must be treated as
113 'minimum' ages due to the potential impact of surface erosion or transient shielding by snow or
114 sediment cover. Two ^{10}Be ages are likely compromised by prior exposure (*inheritance*) and are
115 excluded from further analysis. Sample CAC28 from the Cometa d'Espagne cirque ($26.96 \pm 2.89 \text{ ka}$;
116 Crest et al., 2017) is proximal ($\sim 2 \text{ m}$) to 3 tightly clustered bedrock ages (CAC25 = $10.85 \pm 2.04 \text{ ka}$;
117 CAC26 = $11.97 \pm 1.86 \text{ ka}$; CAC27 = $11.95 \pm 2.92 \text{ ka}$; Mean squared weighted deviation (MSWD) =
118 0.094). Similarly, sample ICM04 from the Malniu catchment (Age = $80.73 \pm 7.92 \text{ ka}$; Pallàs et al.,
119 2010) is proximal ($\sim 10 \text{ m}$) to 3 dated moraine boulders (ICM01 = $51.12 \pm 4.84 \text{ ka}$; ICM02 = $43.91 \pm$
120 4.28 ka ; ICM03 = $42.59 \pm 4.15 \text{ ka}$; MSWD = 0.945). Both of these datasets are internally consistent
121 (MSWD < 1; ICM01-03; CAC25-27), which suggests that prior exposure, rather than post-
122 depositional exhumation, accounts for the positively skewed distribution of ^{10}Be ages. Remaining
123 data ($n = 52$) are used to construct an ordinary least squares (OLS) regression from which numerical
124 ages can be interpolated based on SH R-values.

125 To test for regional variation in rates of sub-aerial weathering, age control data (n = 52) were
126 separated into sub-regions (Fig. 3A; Southern n = 46; Eastern n = 34; Central n = 18). These
127 datasets were used to construct logarithmic regressions for each sub-region. For each sub-region
128 regression, ages were calculated at R-value intervals of 0.1 over the associated calibration period
129 (Southern = 4.1 - 51.1 ka; Eastern = 10.9 - 51.1 ka; Central = 4.1 - 18.2 ka). Interpolated ages were
130 compared to the ages generated by the full age control dataset, with two-sample Students t-tests
131 used to evaluate whether the difference between sub-region and full dataset results was statistically
132 significant. Sub-region information is presented in Table 2.

133 To verify the suitability of this TCN-SH calibration curve, 100 granite surfaces were sampled from 5
134 ice-front positions along a ~18 km transect of the Têt catchment, Eastern Pyrenees (Fig. 4), with
135 results validated against independent ^{10}Be and ^{14}C ages (Delmas et al., 2008) i.e. ^{10}Be ages that do
136 not comprise one of the 52 age control surfaces that underpin the calibration curve (Fig. 1). Of the
137 26 ^{10}Be ages reported by Delmas et al. (2008), many post-date the timing of final deglaciation, likely
138 due to moraine stabilisation processes (Hallet and Putknonen, 1994). Despite this limitation, these
139 data, in addition to geomorphological mapping of moraine stages (Fig. 5), provide a useful
140 chronological framework for ice recession in the Têt catchment and can be used as independent
141 evidence to verify the results of SHED. Sampled sites include proximal inner (Site A, 1 km from
142 catchment headwall, ~2200 m) and outer cirque moraines (Site B, 1.3 km, ~2168 m). Based on
143 existing ^{10}Be ages, these moraines may reflect ice margin oscillations during the Younger Dryas or
144 early-Holocene although considerable age scatter (n = 5; 12.00 - 13.99 ka) prevents accurate
145 separation of glacial stages. Down-valley from these sites, glacially-deposited boulders adjacent to a
146 prominent lateral moraine (Site C, 5.5 km, ~2051 m) are indicative of a post-LGM re-advance of the
147 Têt glacier. This site is down-valley of the Grave-amont core site, which has produced ^{14}C ages in
148 the range 19.47 - 20.26 ka cal BP (n = 3). These data suggest that the Têt glacier was confined to the
149 cirque environment as early as ~20 ka. Further south, a large terminal moraine (Site D, 18.5 km,
150 ~1686 m), dated to 24.22 ± 4.58 ka (n = 1), likely marks the LGM ice extent. ^{10}Be ages from this
151 glacial stage exhibit considerable scatter (n = 6; 15.6 - 24.2 ka) and likely reflect post-depositional

152 exhumation of moraine boulders (Hallet and Putkonen, 1994). As a result, the precise age of this
153 landform is unclear, which limits our understanding of the dynamics of the Têt glacier during the
154 global LGM. Finally, ~300 m outside of the LGM limit, the two outermost moraines of the Têt
155 glacier (Site E, 18.8 km, ~1624 m) mark the Würmian MIE, although the precise age of this landform
156 is unclear. These moraines record the maximum extent of glaciation in the Têt catchment, as the
157 downstream landscape is dominated by fluvial incision. These moraines are morphologically distinct
158 from proximal LGM moraines (Delmas et al. 2008) but it is not currently clear whether these
159 landforms were deposited synchronously, with the outer moraines subject to intense moraine
160 stabilisation processes since the LGM, or instead, whether the outer moraines represent an earlier
161 glacial stage (MIS 3-4; Calvet et al., 2011). At each site, 20 surfaces were sampled for SHED following
162 the methods described above, with SH exposure ages and 1σ uncertainties calculated using SHED-
163 Earth (<http://shed.earth>; Tomkins et al., 2018). To account for geological uncertainty which typically
164 displays as positive and negative skew of datasets, probability density estimates (PDEs) were
165 produced and modelled to separate out the highest probability Gaussian distribution (Fig. 5) as per
166 the methods of Dortch et al. (2013). Using the KS density kernel in MATLAB (2015) and a dynamic
167 smoothing window based on age uncertainty, PDE peaks and tails were separated into individual
168 Gaussian distributions, the sum of which integrates to the cumulative PDE at 1000 iterations to
169 obtain the best fit. The re-integrated PDE (made from the isolated Gaussians) goodness of fit is
170 indicated graphically (Dortch et al., 2013). Full sample information for the 100 surfaces sampled in
171 the Têt catchment can be found in the Supplementary Dataset.

172

173 **RESULTS**

174 A clear correlation between TCN exposure ages and SH R-values is expressed by a logarithmic
175 regression (Fig. 1A; $n = 52$, $R^2 = 0.96$, $p = < 0.01$). Boulder height (Fig. 3B; $n = 38$; $R^2 = < 0.01$; $p =$
176 0.97), sample elevation (Fig. 3C; $R^2 = 0.11$; $p = 0.02$) and cirque headwall distance (Fig. 3D; $R^2 = 0.09$;
177 $p = 0.04$) have a negligible correlation with R-values. Significant differences in R-values between

178 recently exposed surfaces (< 5 ka; R-values > 60) and those exposed during the Younger Dryas (R-
179 values ~ 50), the LGM (R-values ~ 40) and the Würmian MIE (R-values ≤ 30) indicates that age-related
180 information can be retained with carborundum treatment (Moses et al., 2014). There is no significant
181 variation in sub-aerial weathering rate between sub-regions (Table 2; Fig. 3A) as *eastern* ($n = 34$),
182 *central* ($n = 18$) and *southern* curves ($n = 46$) are completely enclosed by the 1σ boundaries of the full
183 dataset curve and generate SH ages that vary from the full dataset by ≤ 0.37 ka, ≤ 0.93 ka and ≤ 0.22
184 ka respectively. In addition, the average sub-region variation from the full dataset is limited to $0.11 \pm$
185 0.06 ka and 0.14 ± 0.08 ka for the *southern* and *eastern* datasets respectively, increasing to $0.43 \pm$
186 0.22 ka for the *central* dataset. This likely reflects the limited calibration period (4.1 - 18.2 ka) and
187 low number of age control surfaces ($n = 18$) for the *central* dataset. As a result, TCN-SH calibration
188 curves should be based on large age control datasets (≥ 25 ^{10}Be ages; Tomkins et al., 2016; 2018) to
189 minimise the effect of individual exposure age errors. Despite this, two-sample Students t-tests
190 indicate that variation between age estimates derived from the full dataset and *southern*, *eastern* and
191 *central* datasets is not statistically significant (Table 2; p values > 0.91).

192 In the Têt catchment, Schmidt Hammer sampling of undated glacially-deposited boulders reveals
193 statistically significant differences (Two-sample Students t-tests, $p < 0.01$) between the mean SH R-
194 values of sequential glacial landforms (A-B, B-C, C-D, D-E). Statistically significant differences in
195 mean SH R-values are evident between both proximal (~ 300 m; A-B; D-E) and distal landforms (~ 13
196 km; C-D). These data were converted into numerical ages based on the TCN-SH calibration curve
197 presented in this paper ($y = 44.02\ln(x) + 186.55$) although these must be considered minimum ages
198 as post-depositional erosion is assumed to be negligible (0 mm ka^{-1}). Incorporating an erosion rate of
199 0.3 mm ka^{-1} (André, 2002) increases calibration ^{10}Be ages ($n = 52$) by $\leq 1.43\%$ and by an average of
200 $\sim 0.64\%$, equivalent to ~ 0.7 ka for sample ICM01 (~ 50 ka) and ≤ 0.16 ka for surfaces exposed within
201 the last ~ 25 ka. This variation is within measurement uncertainty for ^{10}Be ages and is significantly less
202 than the 1σ uncertainty of individual SH exposure ages (Min. = 1.69 ka; Max. = 1.85 ka). As a result,
203 incorporating erosion has a negligible impact on calculated SH exposure ages, even for landforms
204 deposited prior to the LGM. To account for geological uncertainty in interpolated ages, PDE

205 modelling (Dortch et al., 2013) produces peak Gaussian distributions for glacial landforms in the Têt
206 catchment of (A) 9.41 ± 0.62 ka, (B) 12.62 ± 0.91 ka, (C) 16.08 ± 0.46 ka, (D) 24.80 ± 0.90 ka and
207 (E) 40.86 ± 1.09 ka.

208

209 **DISCUSSION**

210 Firstly, a strong correlation between ^{10}Be ages and SH R-values indicates that the primary control on
211 surface R-values is cumulative exposure to sub-aerial weathering (Tomkins et al., 2016; 2018). This
212 correlation is observed despite marked variability in sample elevations (Elevation range = ~ 1836 m),
213 boulder heights (Height = ~ 0.5 to ~ 3.5 m), cirque headwall distances (~ 0.6 to ~ 22 km) and relative
214 positions along the axis of the Pyrenean mountain range (Fig. 1B; Max. distance between samples =
215 ~ 110 km). These data match previous evidence from the British Isles (Tomkins et al., 2016; 2018)
216 and the Krkonoše Mountains, Poland/Czech Republic (Engel, 2007; Engel et al., 2011) for a
217 relationship between ^{10}Be ages and sub-aerial weathering of granite surfaces. However, clear
218 differences in effective calibration timescales in the British Isles (~ 25 ka), the Krkonoše Mountains
219 (~ 15 ka) and the Pyrenees (~ 50 ka) indicates that weathering rates vary significantly between these
220 regions, likely as a function of latitudinal gradients in either precipitation or temperature. The data
221 presented in this study also provide further evidence that weathering rates are not linear but
222 decrease over time (White and Brantley, 2003; Stahl et al., 2013). For surfaces exposed prior to the
223 LGM, slower rates of weathering likely reflect the formation of stable weathering residues which
224 slow water transport to unaltered material and impede chemical transport away from it (Colman,
225 1981). Finally, these data imply little variation in the rate of rock surface weathering between sub-
226 regions over the last ~ 50 ka (Table 2; Fig. 3A). It must be noted that this interpretation is based on
227 the assumption that recalibrated ^{10}Be ages are accurate ages for deglaciation, with no post-
228 depositional erosion. If this assumption is not valid, then variable regional weathering rates could
229 influence ^{10}Be ages and introduce bias to the SHED calibration curve as distal surfaces exposed
230 synchronously could return contrasting ^{10}Be ages. However, under the assumption of minimal

231 weathering of crystalline rock surfaces ($0\text{--}3\text{ mm ka}^{-1}$; André, 2002), post-depositional erosion is
232 unlikely to have significant impact on the results of SHED as differences in ^{10}Be ages due to erosion
233 are significantly smaller than ^{10}Be measurement uncertainty (Sample ICM01; ^{10}Be age uncertainty = \pm
234 4.99 ka ; Age difference $0\text{--}3\text{ mm ka}^{-1}$ erosion = $\sim 0.7\text{ ka}$). This appears to contrast with recent
235 evidence from New Zealand, with marked local variability in rates of rock surface weathering (Stahl
236 et al., 2013). This variability necessitates local calibration curves for proximal sites ($\sim 100\text{ km}$
237 distance) which are applicable over contrasting calibration timescales (Saxton and Charwell River
238 terraces = $\sim 10\text{ ka}$; Waipara River terraces = $\sim 1\text{ ka}$; c.f. Fig. 2 in Stahl et al., 2013). New data from
239 the Pyrenees indicate that sub-aerial weathering of granite surfaces is consistent across the Central
240 and Eastern Pyrenees which implies that equivalent time-dependent weathering of granite surfaces
241 can occur over significant spatial scales for regions of similar climate (Tomkins et al., 2016; 2018).

242 In the Têt catchment, age estimates derived from PDE modelling of Gaussian distributions (Dortch
243 et al., 2013) are in correct stratigraphic order, are consistent with existing interpretations of post-
244 MIE glaciation (Fig. 5) and are supported by independent ^{10}Be ages which provide a chronological
245 framework for the retreat dynamics of the Têt glacier during the Würmian (Delmas et al., 2008).
246 Gaussian ages clearly differentiate LGM (D; $24.80 \pm 0.90\text{ ka}$) and Würmian MIE (E; $40.86 \pm 1.09\text{ ka}$)
247 glacial deposits and provide firm evidence of comparable glacier lengths during MIS 2 and MIS 3
248 ($\sim 300\text{ m}$ difference). This contrasts markedly with evidence from the Western Pyrenees, where
249 glaciers failed to reach MIE limits during the LGM ($\geq 15\text{ km}$ difference; Gállego catchment; Jalut et al.,
250 1992; Calvet et al., 2011). The proximity of MIE and LGM deposits matches the geomorphological
251 record in Malniu ($\sim 330\text{ m}$) and Querol ($\sim 600\text{ m}$) and indicates that glaciers in the Eastern Pyrenees
252 advanced significantly during MIS 2 to near MIE limits, irrespective of glacier size (Querol: $\sim 25\text{ km}$,
253 Têt: $\sim 18.5\text{ km}$, Malniu: $\sim 6\text{ km}$). A MIS 3 Würmian MIE ($40.86 \pm 1.09\text{ ka}$) matches ages from a
254 terminal moraine in Malniu (TCN; $n = 3$; $42.6\text{--}51.1\text{ ka}$; Pallàs et al., 2010), a mid-valley lateral
255 moraine in the Ariege (TCN; $n = 1$; $37.89 \pm 9.98\text{ ka}$; Delmas et al., 2011) and OSL ages from the
256 Senegüe terminal moraine in the Gállego catchment ($n = 2$; $\sim 36\text{ ka}$; Lewis et al., 2009). These data
257 contrast with MIS 4 ages from ice-contact lake deposits in the Cinca catchment (OSL; $n = 3$; $46\text{--}71$

258 ka; Lewis et al., 2009) and from the terminal moraine in the Ariège catchment (TCN; $n = 1$; $88.78 \pm$
259 18.37 ka; Delmas et al., 2011). Regardless of the precise timing of the MIE, one of the most valuable
260 contributions of SHED is its ability to differentiate proximal LGM and MIE glacial deposits and thus,
261 enable robust comparison of glacier length fluctuations across the Pyrenees.

262 By comparison, the timing of the local MIS 2 glacial maximum in the Têt catchment is constrained by
263 both TCN ($n = 1$; 24.22 ± 4.58 ka) and SHED ages ($n = 13$; 24.80 ± 0.90 ka). These data accord with
264 recent evidence that ice masses in the European Alps reached their maximum extents at 24-26 ka
265 due to the growth of the Laurentide Ice Sheet, which reached its maximum close to this time (>23.0
266 ± 0.6 ka; Ullman et al., 2015), and the southward advection of the polar front (Monegato et al.,
267 2017). These events coincided with reduced solar radiation towards the solar minimum in the
268 northern hemisphere at ~ 24 ka (Alley et al., 2002). In addition to SHED and TCN ages from the Têt
269 catchment, an Alpine LGM is supported by post-maximum TCN ages from Querol (YRA Samples; n
270 $= 3$; $22.7 - 24.2$ ka), the oldest ages from the frontal lobe (OEC01; 23.8 ± 2.3 ka) and a coeval lateral
271 moraine (LAF04; 25.7 ± 2.7 ka) in Malniu (Pallàs et al., 2010), and ^{14}C ages from the Gállego
272 catchment, which indicate that the MIS 2 MIE occurred by 24.21 ka cal. BP (Jalut et al., 1992). The
273 asynchronicity of Alpine glaciers and the Eurasian ice sheets at the global LGM, the latter reaching its
274 maximum extent at ~ 21 ka (Hughes et al., 2016), demonstrates the sensitivity of Alpine ice masses
275 to the advection of moisture from the Mediterranean Sea (Luetscher et al., 2015). The contrasting
276 size of Pyrenean glaciers at the LGM likely reflects the relative influence of weather systems from
277 the Atlantic and the western Mediterranean, the latter favouring cyclogenesis, convection of moist
278 air and increased precipitation to coastal mountain ranges (Kuhlemann et al., 2008). However, this
279 hypothesis is tentative owing to limited geochronological data for MIS 2 glaciers in the Western
280 Pyrenees. SHED is a viable method to address this knowledge gap as the calibration curve is well
281 constrained by age control points which span the global LGM and is able to reproduce the LGM
282 TCN age in the Têt catchment, varying by <0.6 ka.

283 Finally, the geomorphological record indicates that post-LGM retreat was dynamic (Fig. 5; Borde and
284 Cirque Stages). A number of re-advance events are captured by SHED, with moraines deposited

285 during the Oldest Dryas (C: 16.08 ± 0.46 ka), Younger Dryas (B: 12.62 ± 0.91 ka) and early-
286 Holocene (A: 9.41 ± 0.62 ka). Evidence for a significant re-advance during the Oldest Dryas is
287 matched by TCN ages from the Orri (CPM; $n = 3$; 16.41 ± 0.58 ka) and Malniu catchments (IMA; $n =$
288 5 ; 16.68 ± 0.52 ka) and is consistent with evidence for major advances in the Western Pyrenees
289 (Palacios et al., 2017). However, these data conflict markedly with ^{14}C ages from the Grave-amont
290 core site (Fig. 5; $19.47 - 20.26$ ka cal BP) which indicate rapid post-LGM retreat (~ 3.3 km ka^{-1}). New
291 SHED data indicates that this deposit must have been overridden (Delmas et al., 2008; Crest et al.,
292 2017). In addition, SHED clearly differentiates proximal (~ 300 m) Younger Dryas (YD; B, $12.62 \pm$
293 0.91 ka) and Holocene moraines (A, 9.41 ± 0.62 ka). TCN exposure ages from the YD moraine
294 (Sample N; 12.0 ± 2.2 ka) and proximal bedrock surfaces (Sample O2; 13.4 ± 2.1 ka) give contrasting
295 age estimates but are broadly consistent with the SHED estimate. The age of the inner cirque
296 moraine (A) overlaps with the 9.3 ka event (Rasmussen et al., 2014) although complete deglaciation
297 and re-advance of ice in the Têt catchment after the YD seems unlikely owing to the short-
298 timeframe of this cooling event (~ 110 yr). Instead, this moraine likely marks a standstill or re-
299 advance of the ice margin from sheltered cirques below Pic Cometa d'Espagne. These data in their
300 totality indicate that cirque (A-B) and valley moraines (C) reflect still-stands or re-advances of the
301 Têt glacier, potentially in response to North Atlantic climate fluctuations (OD, YD, 9.3 ka event).
302 These glacial deposits provide a valuable record of ice margin fluctuations and yet the post-LGM
303 history of the Pyrenean icefield is currently poorly understood (Calvet et al., 2011). Future research
304 using SHED must seek to accurately differentiate post-LGM ice masses to provide robust
305 information on the response of these glaciers to North Atlantic climate variability.

306 This new SHED calibration curve demonstrates that this method can be applied successfully in
307 contrasting climatic regimes and that equivalent time-dependent weathering of granite surfaces can
308 occur within regions of similar climate (Tomkins et al., 2016; 2018). TCN-SH calibration curves
309 based on significant age-controls datasets ($n \geq 50$) have been shown to produce robust ages for
310 glacial landforms, as demonstrated through comparison with independent radiometric ages (^{10}Be),
311 and in aggregate, can generate results of comparable accuracy and precision to TCN dating. This

312 approach could be replicated in similar well-dated granite regions throughout the world (e.g.
313 Himalaya, Patagonia, Sierra Nevada) and has the ability to revolutionise high-sample low-budget
314 quantitative studies in Quaternary Science. In the Pyrenees, future applications of SHED are needed
315 to (1) separate LGM and Würmian MIE landforms across the mountain range and to (2) address gaps
316 in our understanding of post-LGM retreat (Calvet et al., 2011). The relative scarcity of
317 geochronological data, particularly in the Western Pyrenees, has thus far prevented a Pyrenean-scale
318 synthesis of post-MIS 4 glaciation, although progress continues to be made (e.g. Palacios et al., 2017).
319 Widespread application of SHED across the Pyrenees would generate a wealth of new chronological
320 data related to glacier oscillations over the last ~50 ka and would likely accelerate progress in our
321 understanding of the last Pleistocene glacial cycle.

322 To apply this regional calibration curve to undated landforms or to verify its accuracy on landforms
323 dated using radiometric methods (TNC, OSL, ^{14}C), users should follow the methods described
324 above and perform (1) instrument calibration and (2) age calibration procedures as described fully in
325 Tomkins et al. (2018). To perform instrument calibration, users should sample a suitable surface
326 before and after data collection which returns R-values which lie within the range of R-values
327 measured in the field (Tomkins et al., 2018). In contrast, instrument calibration using the test anvil
328 (R-value = 81 ± 2 ; Proceq, 2004) is inappropriate for surfaces typically tested by Quaternary
329 researchers (R-values: 25 - 60) and should only be utilised for the hardest natural rock surfaces (R-
330 values ≥ 70). To perform age calibration and to standardise different Schmidt Hammers and different
331 user strategies to the Pyrenean calibration curve, users should test their Schmidt Hammer on one of
332 three calibration surfaces provided (Mean of 30 R-values; Table 3; Sample photos available at
333 <http://shed.earth>) rather than the University of Manchester calibration boulder as described in
334 Dortch et al. (2016). Users should compare the recorded mean R-value against the assigned value
335 (Table 3) to calculate a correction factor which is then all applied to user data. This functionality is
336 incorporated into SHED-Earth. These procedures facilitate comparison between studies and
337 encourage wider and more consistent application of SHED throughout the Pyrenees.

338

340 CONCLUSIONS

341 Quaternary deposits in the Pyrenees are ideally placed for paleoclimate studies given their proximity
342 to both the North Atlantic and the Mediterranean. However, limited geochronological datasets, the
343 increasing fragmentation of trunk glaciers, and the incomplete nature of the geomorphological
344 record, have prevented a regional scale synthesis of post-MIS 4 glaciation. The Pyrenees are ideally
345 suited for Schmidt Hammer exposure dating (SHED) given the excellent preservation of glacial
346 deposits and the abundance of granite glacial boulders and erosion surfaces.

347 In this study, we show that SHED is a viable geochronological technique, as a strong correlation
348 between 52 TCN exposure ages and SH R-values ($R^2 = 0.96$, $p < 0.01$) permits the use of the SH as
349 a numerical dating tool. The effectiveness of this method is demonstrated for the Têt catchment in
350 the Eastern Pyrenees, where SH exposure ages are in correct stratigraphic order, are consistent
351 with existing geomorphological interpretations, and show excellent agreement with previous TCN
352 ages. SHED data confirm comparable glacier lengths during the LGM and the MIE in the Eastern
353 Pyrenees (~300 m), in contrast to evidence from the Western Pyrenees (>15 km), and also confirm
354 the antiquity of the MIE which likely occurred during MIS 3 (40.86 ± 1.09 ka). Moreover, SHED data
355 show that glaciers in the Eastern Pyrenees reached their maximum extents during the global LGM,
356 synchronous with Alpine ice masses (24 - 26 ka). Glacier expansion was driven by enhanced
357 moisture availability caused by southward advection of the polar front coinciding with the maximum
358 extent of the Laurentide Ice Sheet and a solar minimum at ~24 ka.

359 SHED is cost and time-efficient and can differentiate proximal glacial deposits (~300 m) and in
360 aggregate, can generate results of comparable accuracy and precision to TCN dating. Moreover, our
361 approach provides new evidence for non-linear weathering of granitic surfaces through time, likely
362 associated with the formation of stable weathering residues. Finally, our data imply little variation in

363 the rate of sub-aerial weathering between sub-regions over the last ~50 ka, which indicates that our
364 calibration curve can be applied widely throughout the Central and Eastern Pyrenees.

365

366 **ACKNOWLEDGMENTS**

367 This project was supported by the Royal Geographical Society (with IBG) with a Dudley Stamp
368 Memorial Award and by the University of Manchester SEED Fieldwork Support Fund. Dortch,
369 Hughes and Huck would like to thank the University of Manchester Research Stimulation Fund. We
370 would also like to thank Prof. John Matthews, associate editor Prof. James Shulmeister and an
371 anonymous reviewer for their constructive reviews.

372 **REFERENCES**

373 Alley, R. B., Brook, E. J., & Anandakrishnan, S. (2002). A northern lead in the orbital band: north–
374 south phasing of Ice-Age events. *Quaternary Science Reviews*, 21(1), 431–441.

375 [https://doi.org/10.1016/S0277-3791\(01\)00072-5](https://doi.org/10.1016/S0277-3791(01)00072-5)

376 André, M. F. (2002). Rates of postglacial rock weathering on glacially scoured outcrops (Abisko–
377 Riksgränsen Area, 68°N). *Geografiska Annaler, Series A: Physical Geography*, 84, 139–150.

378 <https://doi.org/10.1111/j.0435-3676.2002.00168.x>

379 Balco, G., Stone, J. O., Lifton, N. A., & Dunai, T. J. (2008). A complete and easily accessible means of
380 calculating surface exposure ages or erosion rates from ¹⁰Be and ²⁶Al measurements.

381 *Quaternary Geochronology*, 3, 174–195. <https://doi.org/10.1016/j.quageo.2007.12.001>

382 Barr, I. D., Roberson, S., Flood, R., & Dortch, J. (2017). Younger Dryas glaciers and climate in the
383 Mourne Mountains, Northern Ireland. *Journal of Quaternary Science*, 32(1), 104–115.

384 <https://doi.org/10.1002/jqs.2927>

385 Borchers, B., Marrero, S., Balco, G., Caffee, M., Goehring, B., Lifton, N., Nishiizumi, K., Phillips, F.,

386 Schaefer, J., & Stone, J. (2016). Geological calibration of spallation production rates in the
387 CRONUS- Earth project. *Quaternary Geochronology*, 31, 188–198.
388 <https://doi.org/10.1016/j.quageo.2015.01.009>

389 Calvet, M., Delmas, M., Gunnell, Y., & Bourle, D. (2011). Recent Advances in Research on
390 Quaternary Glaciations in the Pyrenees. In J. Ehlers, P. L. Gibbard, & P. D. Hughes (Eds.),
391 *Quaternary Glaciations, Extent and Chronology, a closer look Part IV* (Vol. 15, pp. 127–139). Elsevier.
392 <https://doi.org/10.1016/B978-0-444-53447-7.00011-8>

393 Černá, B., & Engel, Z. (2011). Surface and sub-surface Schmidt hammer rebound value variation for a
394 granite outcrop. *Earth Surface Processes and Landforms*, 36, 170-179.
395 <https://doi.org/10.1002/esp.2029>

396 Colman, S. M. (1981). Rock-Weathering Rates as Functions of Time. *Quaternary Research*, 264(15),
397 250–264. [https://doi.org/10.1016/0033-5894\(81\)90029-6](https://doi.org/10.1016/0033-5894(81)90029-6)

398 Crest, Y., Delmas, M., Braucher, R., Gunnell, Y., Calvet, M., & ASTER Team. (2017). Cirques have
399 growth spurts during deglacial and interglacial periods: Evidence from ¹⁰Be and ²⁶Al nuclide
400 inventories in the central and eastern Pyrenees. *Geomorphology*, 278, 60–77.
401 <https://doi.org/10.1016/j.geomorph.2016.10.035>

402 Delmas, M. (2015). The last maximum ice extent and subsequent deglaciation of the Pyrenees: an
403 overview of recent research. *Cuadernos de Investigación Geográfica*, 41, 109-137.
404 <http://dx.doi.org/10.18172/cig.2708>

405 Delmas, M., Gunnell, Y., Braucher, R., Calvet, M., & Bourlès, D. (2008). Exposure age chronology of
406 the last glaciation in the eastern Pyrenees. *Quaternary Research*, 69, 231–241.
407 <https://doi.org/10.1016/j.yqres.2007.11.004>

408 Delmas, M., Calvet, M., Gunnell, Y., Braucher, R., & Bourlès, D. (2011). Palaeogeography and ¹⁰Be
409 exposure-age chronology of Middle and Late Pleistocene glacier systems in the northern
410 Pyrenees: Implications for reconstructing regional palaeoclimates. *Palaeogeography*,

411 *Palaeoclimatology, Palaeoecology*, 305(1–4), 109–122. <https://doi.org/10.1016/j.palaeo.2011.02.025>

412 Delmas, M., Braucher, R., Gunnell, Y., Guillou, V., Calvet, M., & Bourlès, D. (2015). Constraints on
413 Pleistocene glaciofluvial terrace age and related soil chronosequence features from vertical ¹⁰Be
414 profiles in the Ariège River catchment (Pyrenees, France). *Global and Planetary Change*, 132, 39-
415 53. <https://doi.org/10.1016/j.gloplacha.2015.06.011>

416 Dortch, J. M., Owen, L. A., & Caffee, M. W. (2013). Timing and climatic drivers for glaciation across
417 semi-arid western Himalayan-Tibetan orogen. *Quaternary Science Reviews*, 78, 188–208.
418 <https://doi.org/10.1016/j.quascirev.2013.07.025>

419 Dortch, J. M., Hughes, P.D., & Tomkins, M. D. (2016) Schmidt hammer exposure dating (SHED):
420 Calibration boulder of Tomkins et al. (2016). *Quaternary Geochronology*, 35, 67-68.
421 <https://doi.org/10.1016/j.quageo.2016.06.001>

422 Engel, Z. (2007). Measurement and age assignment of intact rock strength in the Krkonoše
423 Mountains, Czech Republic. *Zeitschrift für Geomorphologie*, 51, 69-80.
424 <https://doi.org/10.1127/0372-8854/2007/0051S-0069>

425 Engel, Z., Traczyk, A., Braucher, R., Woronko, B., & Krížek, M. (2011). Use of ¹⁰Be exposure ages
426 and Schmidt hammer data for correlation of moraines in the Krkonoše Mountains,
427 Poland/Czech Republic. *Zeitschrift für Geomorphologie*, 55(2), 175-196.
428 <https://doi.org/10.1127/0372-8854/2011/0055-0036>

429 Gunnell, Y., Calvet, M., Brichau, S., Carter, A., Aguilar, J.-P., & Zeyen, H. (2009). Low long-term
430 erosion rates in high-energy mountain belts: insights from thermo- and biochronology in the
431 Eastern Pyrenees. *Earth and Planetary Science Letters*, 278, 208-218.
432 <https://doi.org/10.1016/j.epsl.2008.12.004>

433 Hallet, B., & Putkonen, J. (1994). Surface Dating of Dynamic Landforms: Young Boulders on Aging
434 Moraines. *Science*, 265(5174), 937–940. <http://doi.org/10.1126/science.265.5174.937>

435 Heyman, J., Stroeve, A. P., Harbor, J. M., & Caffee, M. W. (2011). Too young or too old: Evaluating
436 cosmogenic exposure dating based on analysis of compiled boulder exposure ages. *Earth and*
437 *Planetary Science Letters*, 302(1-2), 71-80. <https://doi.org/10.1016/j.epsl.2010.11.040>

438 Hughes, P. D., & Gibbard, P. L. (2015). A stratigraphical basis for the Last Glacial Maximum (LGM).
439 *Quaternary International*, 383, 174-185. <https://doi.org/10.1016/j.quaint.2014.06.006>

440 Hughes, A. L., Gyllencreutz, R., Lohne, Ø. S., Mangerud, J., & Svendsen, J. I. (2016). The last Eurasian
441 ice sheets—a chronological database and time-slice reconstruction, DATED-1. *Boreas*, 45(1), 1-
442 45. <https://doi.org/10.1111/bor.12142>

443 Jalut, G., Monserrat Marti, J., Fontugne, M., Delibrias, G., Vilaplana, J. M., & Julia, R. (1992). Glacial to
444 interglacial vegetation changes in the northern and southern Pyrenees: deglaciation, vegetation
445 cover and chronology. *Quaternary Science Reviews*, 11, 449–480. [https://doi.org/10.1016/0277-](https://doi.org/10.1016/0277-3791(92)90027-6)
446 [3791\(92\)90027-6](https://doi.org/10.1016/0277-3791(92)90027-6)

447 Katz, O., Reches, Z., & Roegiers, J.-C. (2000). Evaluation of mechanical rock properties using the
448 Schmidt Hammer. *International Journal of Rock Mechanics and Mining Sciences*, 37, 723-728.
449 [https://doi.org/10.1016/S1365-1609\(00\)00004-6](https://doi.org/10.1016/S1365-1609(00)00004-6)

450 Kłapyta, P. (2013). Application of Schmidt hammer relative age dating to Late Pleistocene moraines
451 and rock glaciers in the Western Tatra Mountains, Slovakia. *Catena*, 111, 104-121.
452 <http://dx.doi.org/10.1016/j.catena.2013.07.004>

453 Kuhlemann, J., Rohling, E. J., Krumrei, I., Kubik, P., Ivy-Ochs, S., & Kucera, M. (2008). Regional
454 synthesis of Mediterranean atmospheric circulation during the Last Glacial Maximum. *Science*,
455 321(5894), 1338-1340. <https://doi.org/10.1126/science.1157638>

456 Lal, D. (1991). Cosmic ray labeling of erosion surfaces: in situ nuclide production rates and erosion
457 models. *Earth and Planetary Science Letters*, 104, 424–439. [https://doi.org/10.1016/0012-](https://doi.org/10.1016/0012-821X(91)90220-C)
458 [821X\(91\)90220-C](https://doi.org/10.1016/0012-821X(91)90220-C)

- 459 Lewis, C. J., McDonald, E. V., Sancho, C., Peña, J. L., & Rhodes, E. J. (2009). Climatic implications of
460 correlated Upper Pleistocene glacial and fluvial deposits on the Cinca and Gállego Rivers (NE
461 Spain) based on OSL dating and soil stratigraphy. *Global and Planetary Change*, 67(3–4), 141–152.
462 <https://doi.org/10.1016/j.gloplacha.2009.01.001>
- 463 Luetscher, M., Boch, R., Sodemann, H., Spötl, C., Cheng, H., Edwards, R. L., Frisia, S., Hof, F., &
464 Müller, W. (2015). North Atlantic storm track changes during the Last Glacial Maximum
465 recorded by Alpine speleothems. *Nature Communications*, 6.
466 <https://doi.org/10.1038/ncomms7344>
- 467 Matthews, J. A., & Owen, G. (2008). Endolithic lichens, rapid biological weathering and schmidt
468 hammer r-values on recently exposed rock surfaces: Storbreen glacier foreland, jotunheimen,
469 Norway. *Geografiska Annaler, Series A: Physical Geography*, 90(4), 287–297.
470 <https://doi.org/10.1111/j.1468-0459.2008.00346.x>
- 471 Monegato, G., Scardia, G., Hajdas, I., Rizzini, F., & Piccin, A. (2017). The Alpine LGM in the boreal
472 ice- sheets game. *Scientific Reports*, 7(2078), 1–8. <https://doi.org/10.1038/s41598-017-02148-7>
- 473 Moses, C., Robinson, D., and Barlow, J. (2014). Methods for measuring rock surface weathering and
474 erosion. *Earth-Science Reviews*, 135, 141–161. <http://dx.doi.org/10.1016/j.earscirev.2014.04.006>
- 475 Murari, M.K., Owen, L.A., Dortch, J.M., Caffee, M.W., Dietsch, C., Fuchs, M., Haneberg, W.C.,
476 Sharma, M.C., & Townsend-Small, A. (2014). Timing and climatic drivers for glaciation across
477 monsoon-influenced regions of the Himalayan-Tibetan orogen. *Quaternary Science Reviews*, 88,
478 159–182. <https://doi.org/10.1016/j.quascirev.2014.01.013>
- 479 Niedzielski, T., Migoń, P., & Placek, A. (2009). A minimum sample size required from Schmidt
480 hammer measurements. *Earth Surface Processes and Landforms*, 34, 1713–1725.
481 <https://doi.org/10.1002/esp>
- 482 Ortuño, M., Martí, A., Martín-Closas, C., Jiménez-Moreno, G., Martinetto, E., & Santanach, P. (2013).
483 Palaeoenvironments of the Late Miocene Prüedo Basin: implications for the uplift of the Central

484 Pyrenees. *Journal of the Geological Society*, 170, 79–92. <https://doi.org/10.1144/jgs2011-121>

485 Palacios, D., García-Ruiz, J. M., Andrés, N., Schimmelpfennig, I., Campos, N., Léanni, L., & ASTER
486 Team. (2017). Deglaciation in the central Pyrenees during the Pleistocene–Holocene transition:
487 Timing and geomorphological significance. *Quaternary Science Reviews*, 162, 111–127.
488 <https://doi.org/10.1016/j.quascirev.2017.03.007>

489 Pallàs, R., Rodés, Á., Braucher, R., Bourlès, D., Delmas, M., Calvet, M., & Gunnell, Y. (2010). Small,
490 isolated glacial catchments as priority targets for cosmogenic surface exposure dating of
491 Pleistocene climate fluctuations, southeastern Pyrenees. *Geology*, (10), 891–894.
492 <https://doi.org/10.1130/G31164.1>

493 Pallàs, R., Rodés, Á., Braucher, R., Carcaillet, J., Ortuño, M., Bordonau, J., Bourlès, D., Vilaplana, J. M.,
494 Masana, E., & Santanach, P. (2006). Late Pleistocene and Holocene glaciation in the Pyrenees: a
495 critical review and new evidence from ¹⁰Be exposure ages, south-central Pyrenees. *Quaternary
496 Science Reviews*, 25, 2937–2963. <https://doi.org/10.1016/j.quascirev.2006.04.004>

497 Proceq. (2004). Operating Instructions Betonprüfhammer N/NR- L/LR. Schwerzenbach.

498 Putkonen, J., & Swanson, T. (2003). Accuracy of cosmogenic ages for moraines. *Quaternary Research*,
499 59, 255–261. [https://doi.org/10.1016/S0033-5894\(03\)00006-1](https://doi.org/10.1016/S0033-5894(03)00006-1)

500 Rasmussen, S. O., Bigler, M., Blockley, S. P., Blunier, T., Buchardt, S. L., Clausen, H. B., Cvijanovic, I.,
501 Dahl-Jensen, D., Johnsen, S. J., Fischer, H., Gkinis, V., Guillevic, M., Hoek, W. Z., Lowe, J. J.,
502 Pedro, J. B., Popp, T., Seierstad, I. K., Steffensen, J. P., Svensson, A. M., Vallenga, P., Vinther, B.
503 M., Walker, M. J. C., Wheatley, J. J., & Winstrup, M. (2014). A stratigraphic framework for
504 abrupt climatic changes during the Last Glacial period based on three synchronized Greenland
505 ice-core records: refining and extending the INTIMATE event stratigraphy. *Quaternary Science
506 Reviews*, 106, 14–28. <https://doi.org/10.1016/j.quascirev.2014.09.007>

507 Riebe, C. S., Kirchner, J. W., & Finkel, R. C. (2004). Erosional and climatic effects on long-term
508 chemical weathering rates in granitic landscapes spanning diverse climate regimes. *Earth and*

509 *Planetary Science Letters*, 224, 547–562. <https://doi.org/10.1016/j.epsl.2004.05.019>

510 Stahl, T., Winkler, S., Quigley, M., Bebbington, M., Duffy, B., & Duke, D. (2013). Schmidt hammer
511 exposure-age dating (SHD) of late quaternary fluvial terraces in New Zealand. *Earth Surface
512 Processes and Landforms*, 38(15), 1838-1850. <https://doi.org/10.1002/esp.3427>

513 Stone, J. O. (2000). Air pressure and cosmogenic isotope production. *Journal of Geophysical Research*,
514 105(1), 23753–23759. <https://doi.org/10.1029/2000JB900181>

515 Sumner, P., & Nel, W. (2002). The effect of rock moisture on Schmidt hammer rebound: Tests on
516 rock samples from Marion Island and South Africa. *Earth Surface Processes and Landforms*,
517 27(10), 1137–1142. <https://doi.org/10.1002/esp.402>

518 Tomkins, M. D., Dortch, J. M., & Hughes, P. D. (2016). Schmidt Hammer exposure dating (SHED):
519 Establishment and implications for the retreat of the last British Ice Sheet. *Quaternary
520 Geochronology*, 33, 46–60. <https://doi.org/10.1016/j.quageo.2016.02.002>

521 Tomkins, M. D., Huck, J.J., Dortch, J. M., Hughes, P. D., Kirkbride, M., & Barr, I. (2018). Schmidt
522 Hammer exposure dating (SHED): Calibration procedures, new exposure age data and an
523 online calculator. *Quaternary Geochronology*, 44, 55-62.
524 <https://doi.org/10.1016/j.quageo.2017.12.003>

525 Ullman, D. J., Carlson, A. E., LeGrande, A. N., Anslow, F. S., Moore, A. K., Caffee, M., Syverson, K.
526 M., & Licciardi, J. M. (2015). Southern Laurentide ice-sheet retreat synchronous with rising
527 boreal summer insolation. *Geology*, 43(1), 23-26. <https://doi.org/10.1130/G36179.1>

528 Viles, H., Goudie, A., Grab, S., & Lalley, J. (2011). The use of the Schmidt Hammer and Equotip for
529 rock hardness assessment in geomorphology and heritage science: A comparative analysis.
530 *Earth Surface Processes and Landforms*, 36(3), 320–333. <https://doi.org/10.1002/esp.2040>

531 White, A. F., & Brantley, S. L. (2003). The effect of time on the weathering of silicate minerals: why
532 do weathering rates differ in the laboratory and field? *Chemical Geology*, 202, 479–506.

533 <https://doi.org/10.1016/j.chemgeo.2003.03.001>

534 Williams, R. B. G., & Robinson, D. A. (1983). The effect of surface texture on the determination of
535 the surface hardness of rock using the schmidt hammer. *Earth Surface Processes and*
536 *Landforms*, 8(3), 289–292. <https://doi.org/10.1002/esp.3290080311>

537

538 **Figure Captions**

539 Figure 1. Schmidt Hammer exposure dating (SHED) calibration curve for the Pyrenees. A:
540 Correlation between Schmidt Hammer R-values and terrestrial cosmogenic nuclide (TCN) exposure
541 ages (n = 53). Inherited outlier ICM04 not shown as it is beyond the graph axis (Age = 80.7 ± 7.9 ka,
542 R-value = 24.98 ± 1.17). B: Map of age control sites, sites referred to in text (A: Ariege, C:
543 Campcardós, Ci: Cinca G: Gállego, T: Têt) and the Last Glacial Maximum extent after Calvet et al.
544 (2011).

545 Figure 2. ^{10}Be dated surfaces sampled using the Schmidt Hammer. A: Holocene, B: Younger Dryas,
546 C: Last Glacial Maximum (LGM) and D: Würmian Maximum Ice Extent (MIE) dated surfaces from
547 Pallas et al. (2010) and Crest et al. (2017). Reported ^{10}Be ages were recalibrated using the online
548 calculators formerly known as the CRONUS-Earth online calculators (Balco et al., 2008). Reported
549 R-values are the arithmetic mean of 30 R-values (excluding no outliers) \pm the Standard Error of the
550 Mean (SEM).

551 Figure 3. Local and regional controls on surface R-values. A: Full dataset (*black*) and sub-region
552 calibration curves for the southern (*blue*), eastern (*red*) and central Pyrenees (*green*). Sub-region
553 calibration curves fall within 1σ (dark grey) and 2σ (light grey) prediction limits of the full dataset
554 curve and imply no significant variation in the rate of rock surface weathering between sub-regions.
555 B: Boulder height (m) and surface R-values (n = 38). C: Sample elevation (m) and surface R-values (n
556 = 52). D: Cirque headwall distance (km) and surface R-values (n = 52). These data (A-D) imply that
557 site specific factors have a negligible impact on sub-aerial weathering of granite surfaces in the

558 Central and Eastern Pyrenees.

559 Figure 4. Sampled sites for Schmidt Hammer exposure dating (SHED) from the Têt catchment,
560 Eastern Pyrenees. A: Holocene (Site A; 9.41 ± 0.62 ka) and Younger Dryas moraines (Site B; $12.62 \pm$
561 0.91 ka). B: The prominent lateral moraine and proximal surfaces sampled for SHED (Site C: $16.08 \pm$
562 0.46 ka). C: Sampled surface from the large terminal moraine, previously dated to 24.22 ± 4.58 ka
563 (^{10}Be ; $n = 1$; Delmas et al., 2008), which marks the maximum extent of ice during the Last Glacial
564 Maximum (Site D: 24.80 ± 0.90 ka). D: The outermost moraine of the Têt glacier and the Würmian
565 Maximum Ice Extent for this catchment (Site E: 40.86 ± 1.09 ka).

566 Figure 5. A deglacial chronology for the Têt catchment, Eastern Pyrenees. A: Geomorphological map
567 showing the Würmian Maximum Ice Extent (MIE) for the Têt, Angoustrine and Formiguères glaciers.
568 Moraine stages modified and TCN exposure ages recalibrated from Delmas et al. (2008). Schmidt
569 Hammer sampled sites (A-E) are shown. B: Probability density estimates (PDEs) and Gaussian
570 models for sampled sites (A-E) are plotted against the NGRIP $\delta^{18}\text{O}$ curve (Rasmussen et al., 2014).
571 Key events are shown: Younger Dryas (YD), Oldest Dryas (OD), Global Last Glacial Maximum
572 (GLGM), Local Last Glacial Maximum (LLGM) and the Eurasian Last Glacial Maximum (ELGM).

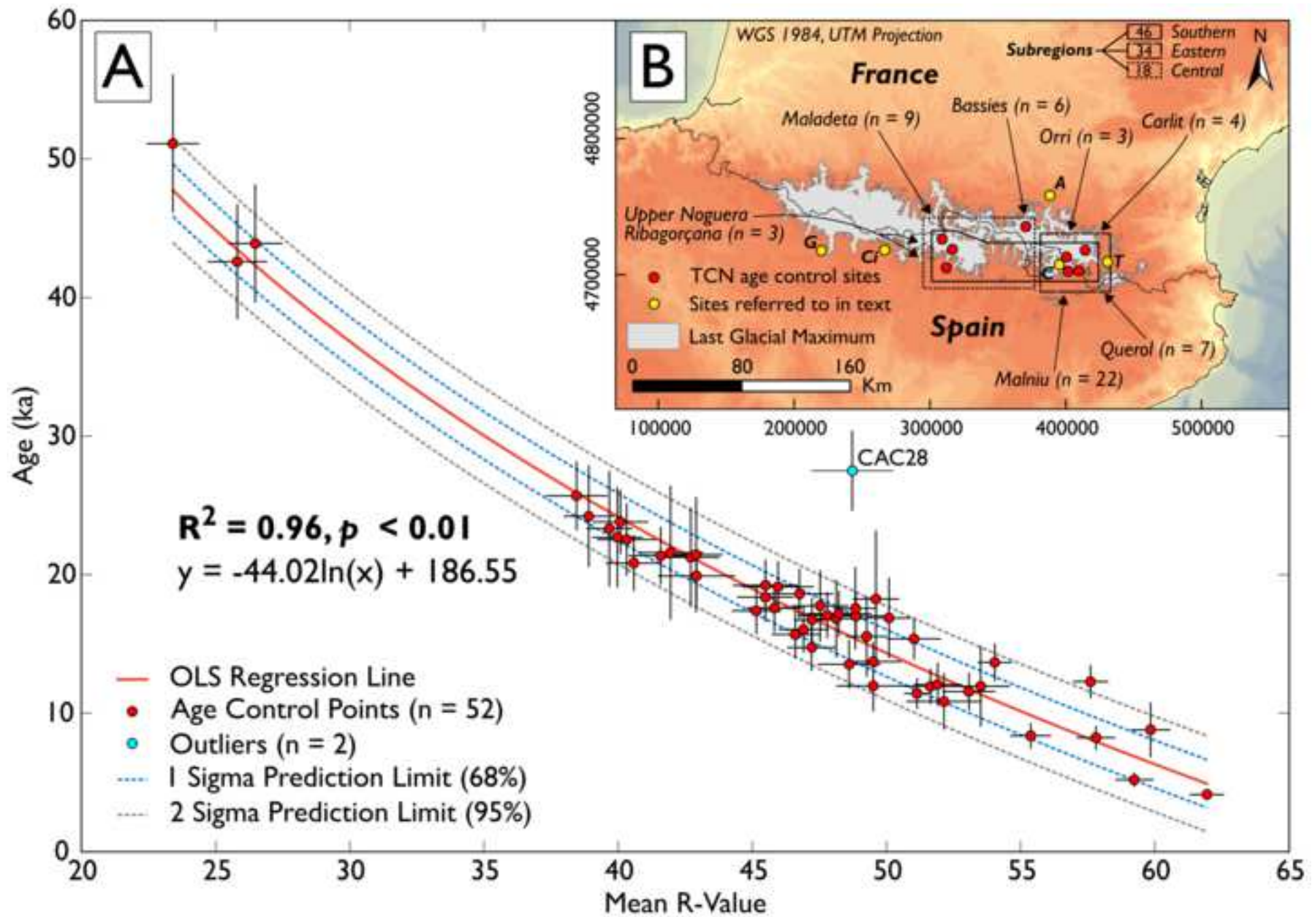
573 **Table Captions**

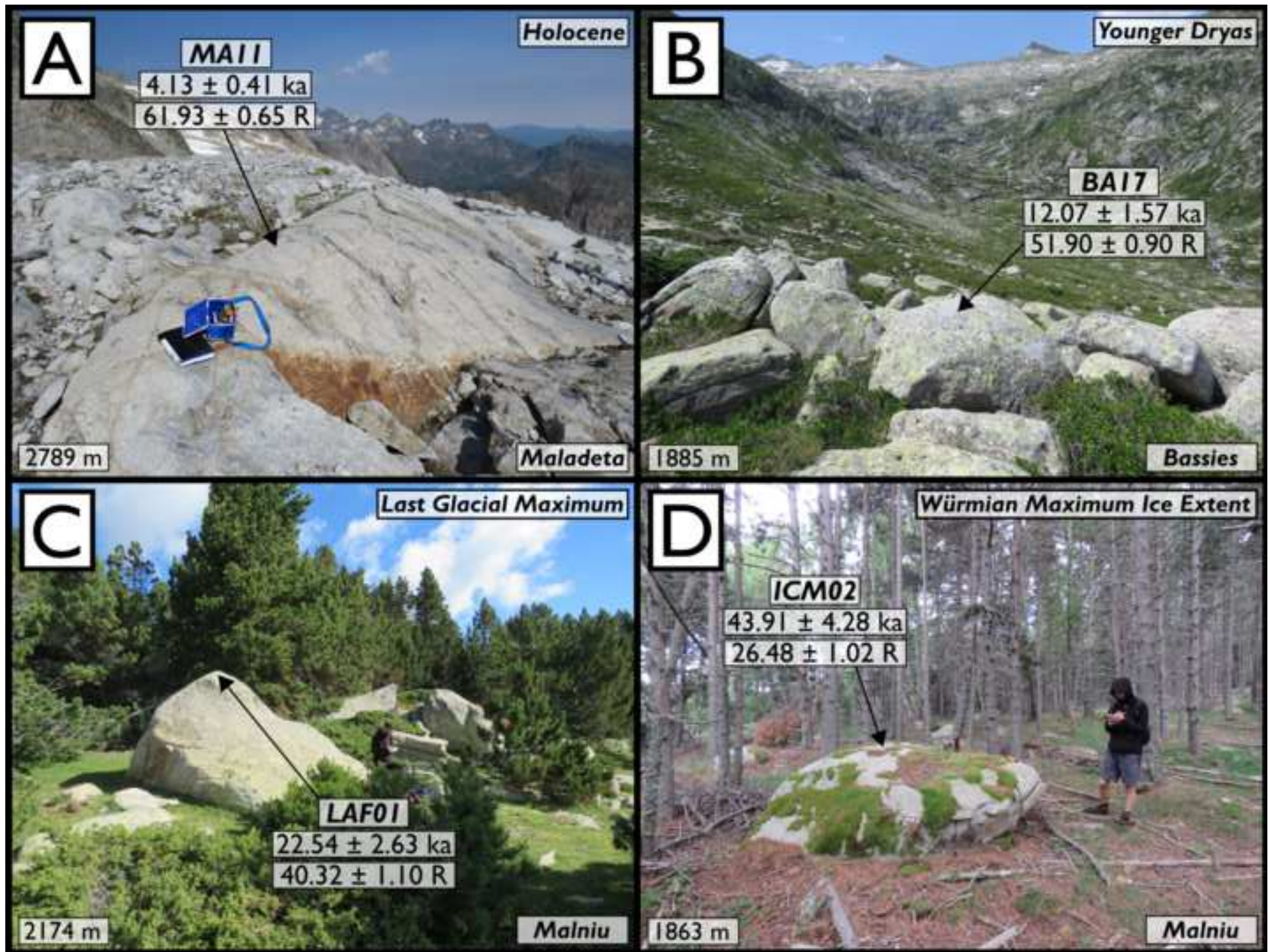
574 Table 1. Details of ^{10}Be dated surfaces sampled using the Schmidt Hammer.

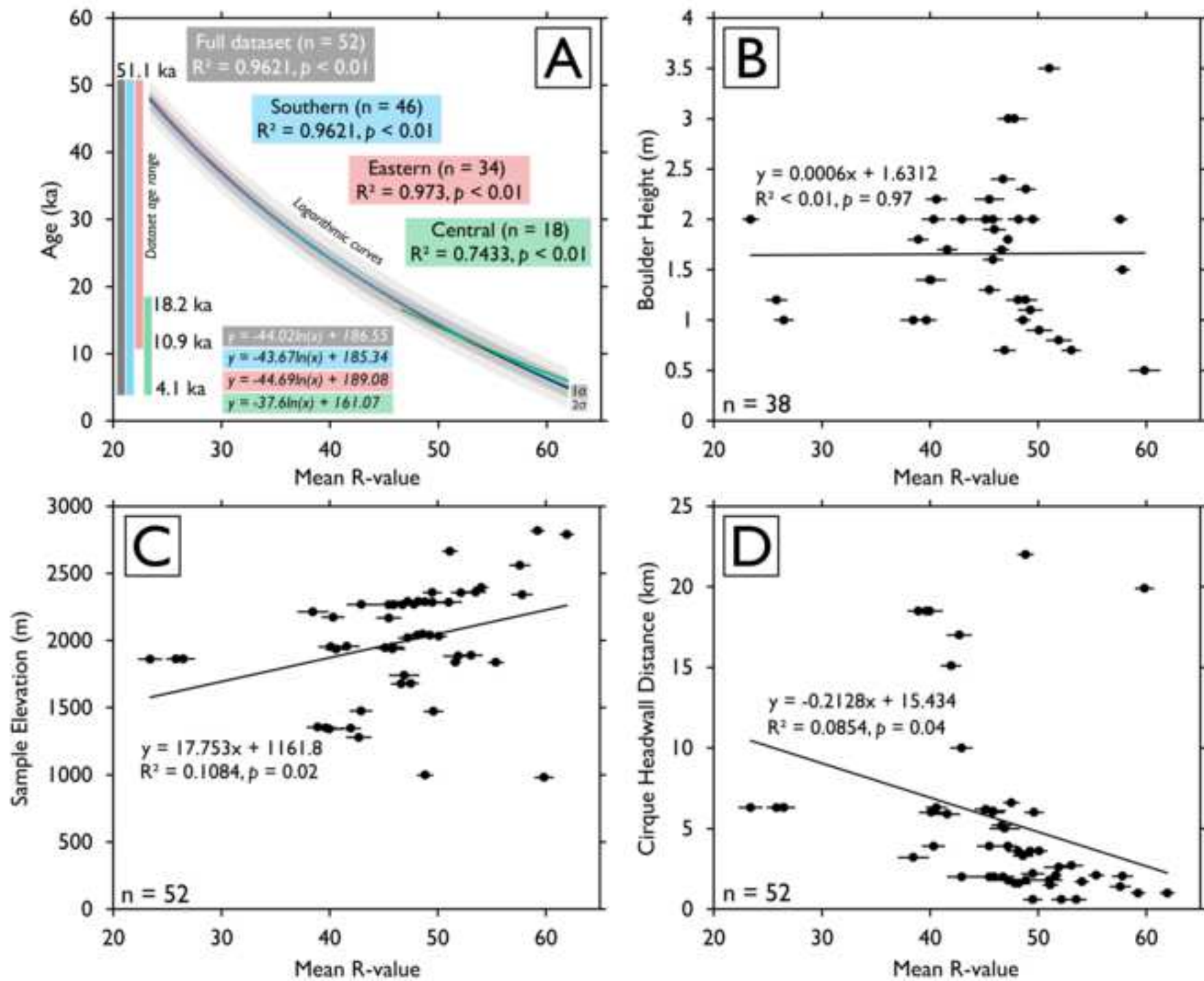
575 Table 2. Analysis of sub-region datasets and comparison with the full age control dataset ($n = 52$).

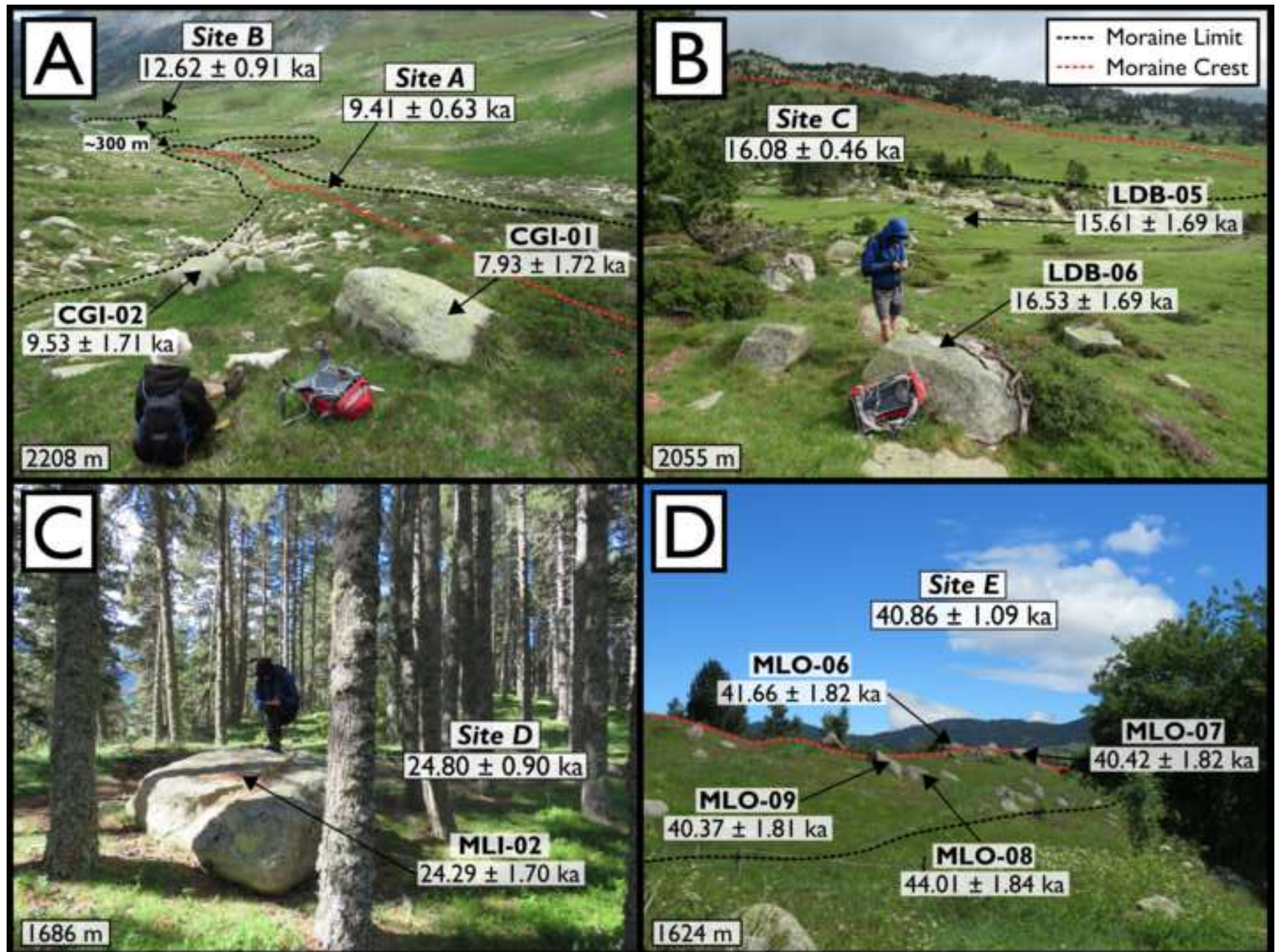
576 These data imply little variation in the rate of sub-aerial weathering between sub-regions.

577 Table 3. Age calibration surfaces for the Pyrenees. Detailed information on age calibration can be
578 found in Tomkins et al. (2018) or at <http://shed.earth>. Users should test their Schmidt Hammer on
579 one of these calibration surfaces provided (Mean of 30 R-values) and input their results into the
580 SHED-Earth online calculator. Age calibration standardises different Schmidt Hammers and user
581 strategies to the regional calibration curve.









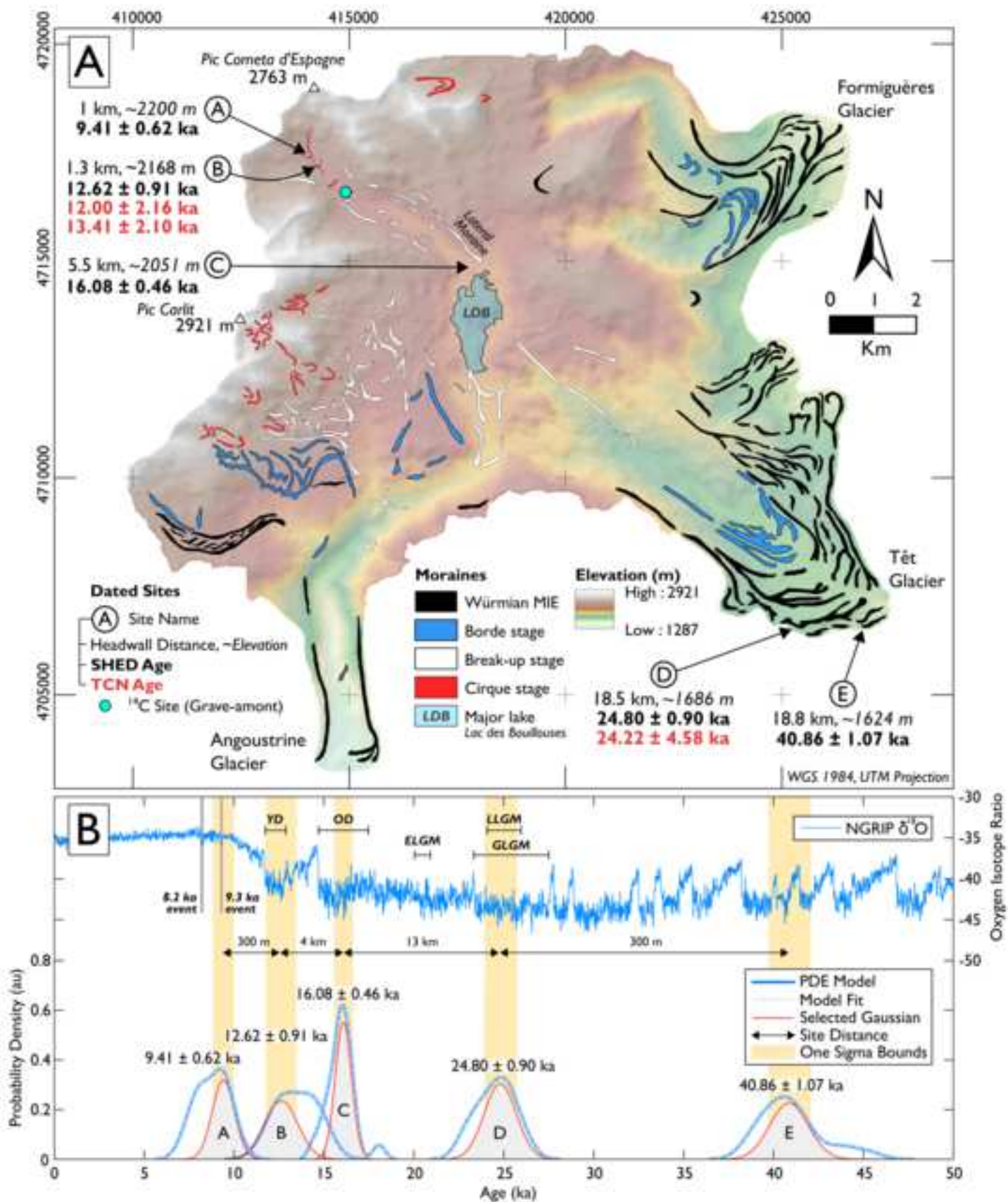


Table 1

Sample	Coordinates ^a	Elevation (m)	Type	Sub-region ^b	Boulder height (m)	Cirque distance (km)	Mean R-Value	SEM ^c	Age (ka)	Io
MA03	306645 4726398	2396	Bedrock	S + C	-	1.7	54.03	0.65	13.67	1.36
MA04	306659 4725978	2560	Boulder	S + C	2	1.4	57.60	0.67	12.29	1.21
MA11	306498 4725387	2789	Bedrock	S + C	-	1	61.93	0.65	4.13	0.41
MA12	306627 4725290	2817	Bedrock	S + C	-	1	59.23	0.71	5.21	0.52
MA07	306901 4725631	2665	Bedrock	S + C	-	1.5	51.13	0.49	11.43	1.12
MA05	306959 4726408	2342	Boulder	S + C	1.5	2.05	57.80	0.73	8.24	0.88
MA06	306991 4726657	2283	Boulder	S + C	2	2.2	49.50	1.04	13.73	1.41
AN02	308872 4726401	2050	Boulder	S + C	1	3.3	48.60	1.18	13.54	1.77
AN01	308669 4726819	2020	Boulder	S + C	1.8	3.9	47.20	0.91	14.74	1.69
STA01	311923 4704290	998	Boulder	S + C	1.2	22	48.84	0.82	17.58	2.98
SMV01	312411 4706093	981	Boulder	S + C	0.5	19.9	59.84	0.74	8.80	1.99
RHL01	316483 4718607	1472	Bedrock	S + C	-	6	49.60	0.87	18.25	4.95
BA15	371797 4735829	1678	Boulder	C	1.7	5.2	46.60	0.89	15.69	1.74
BA16	371426 4736078	1741	Boulder	C	0.7	5	46.90	0.94	16.05	1.69
BA20	369354 4734473	1837	Bedrock	C	-	2.10	51.64	0.95	11.94	1.29
BA19	369354 4734473	1837	Bedrock	C	-	2.1	55.37	0.76	8.38	0.93
BA17	369697 4734705	1885	Boulder	C	0.8	2.6	51.90	0.90	12.07	1.57
BA18	369717 4734785	1890	Boulder	C	0.7	2.7	53.07	0.99	11.57	1.37
FUL03	403443 4707445	1476	Bedrock	S + E	-	10	42.90	0.99	21.45	4.17
LAT01	408106 4702521	1279	Bedrock	S + E	-	17	42.70	1.07	21.26	3.59
YRA-21	408727 4701033	1341	Boulder	S + E	1.4	18.5	39.97	0.94	22.69	3.62
YRA-20	408719 4701031	1349	Boulder	S + E	1	18.5	39.67	0.86	23.32	4.19
YRA-19	408651 4701040	1354	Boulder	S + E	1.8	18.5	38.90	0.94	24.22	3.67
CAC25	414113 4718126	2356	Bedrock	S + E	-	0.6	52.14	1.41	10.85	2.04
CAC26	414113 4718126	2357	Bedrock	S + E	-	0.6	49.51	1.38	11.97	1.85
CAC27	414113 4718126	2360	Bedrock	S + E	-	0.6	53.51	1.09	11.95	2.92
CAC28	414113 4718126	2356	Bedrock	-	-	0.6	48.71	1.53	26.93 ^d	2.89
QRS01	406616 4703876	1346	Bedrock	S + E	-	15.1	41.95	1.21	21.59	4.84
ICM01	404800 4702660	1861	Boulder	S + E	2	6.3	23.41	0.98	51.11	4.99
ICM02	404787 4702624	1863	Boulder	S + E	1	6.3	26.48	1.02	43.91	4.28
ICM03	404764 4702592	1863	Boulder	S + E	1.2	6.3	25.81	1.12	42.59	4.15
ICM04	404736 4702569	1864	Boulder	-	1.5	6.3	24.98	1.17	80.73 ^d	7.92
OEC5	404606 4702925	1935	Boulder	S + E	2.2	6.3	40.58	1.06	20.84	2.04
OEC4	404545 4702828	1945	Boulder	S + E	2	6.2	45.15	0.92	17.39	1.70
OEC6	404548 4703058	1937	Boulder	S + E	1.6	6.1	45.82	0.98	17.58	1.73
OEC3	404415 4702566	1951	Boulder	S + E	2	6	45.82	1.02	17.61	1.74
OEC2	404329 4702532	1956	Boulder	S + E	1.7	5.9	41.58	1.20	21.37	2.09
OEC1	404402 4702668	1953	Boulder	S + E	1.4	6	40.08	1.03	23.81	2.32
LAF03	402597 4701952	2168	Boulder	S + E	2.2	3.9	45.49	1.22	19.23	1.87
LAF01	402493 4701917	2174	Boulder	S + E	2	3.9	40.32	1.10	22.54	2.63
LAF04	401565 4701602	2213	Boulder	S + E	1	3.2	38.45	1.15	25.69	2.50
OMA04	400874 4702314	2267	Boulder	S + E	1.3	2	45.49	1.05	18.38	1.79
OMA02	400871 4702326	2268	Boulder	S + E	2	2	42.92	1.44	19.91	1.93
OMA03	400877 4702330	2267	Boulder	S + E	2.4	2	46.76	1.26	18.62	1.81
OMA01	400884 4702332	2267	Boulder	S + E	1.9	2	45.95	1.34	19.13	1.86
IMA03	400931 4703060	2287	Boulder	S + E	2.3	1.8	48.86	1.07	17.02	1.66
IMA01	400943 4703050	2289	Boulder	S + E	3	1.8	47.22	0.68	16.72	1.63
IMA02	400924 4703031	2286	Boulder	S + E	3.5	1.8	51.02	1.01	15.37	1.50
IMA04	401069 4703262	2270	Boulder	S + E	3	1.6	47.79	1.09	17.08	1.66
IMA05	401073 4703284	2290	Boulder	S + E	2	1.6	48.22	1.22	17.19	1.67
CPM03	400965 4712601	2032	Boulder	S + E	0.9	3.6	50.09	0.82	16.87	2.91
CPM01	400805 4712550	2039	Boulder	S + E	1.2	3.6	48.12	1.09	16.83	2.81
CPM02	400809 4712566	2038	Boulder	S + E	1.1	3.6	49.26	0.76	15.54	2.90
CAS03	403474 4710840	1681	Bedrock	S + E	-	6.6	47.52	1.05	17.75	2.59

^a with reference to WGS 1984 31 T, ^b S = Southern, C = Central, E = Eastern, ^c Standard Error of the Mean, ^d Inherited surface

Table 2

Region	# ages	Age Range (ka)	R-Value Range ^a	Regression Equation	R ²	p value	Mean variation ^b	Mean uncertainty ^c	Max. variation	p value ^d	Interpretation ^e
Full Dataset	52	4.1 - 51.1	25 - 60	$y = -44.02\ln(x) + 186.55$	0.9621	< 0.01	-	1.725 ± 0.031	-	-	-
Southern	46	4.1 - 51.1	25 - 60	$y = -43.67\ln(x) + 185.34$	0.9621	< 0.01	0.11 ± 0.06 ka	1.725 ± 0.031	0.22 ka	0.91	H ₀
Eastern	34	10.9 - 51.1	25 - 54	$y = -44.69\ln(x) + 189.08$	0.973	< 0.01	0.14 ± 0.08 ka	1.728 ± 0.036	0.37 ka	0.92	H ₀
Central	18	4.1 - 18.2	46 - 60	$y = -37.6\ln(x) + 161.07$	0.7433	< 0.01	0.43 ± 0.22 ka	1.704 ± 0.008	0.90 ka	0.98	H ₀

^a Ages interpolated at R-value interval of 0.1 within these ranges, ^b Mean variation from Full Dataset ± Mean Absolute Deviation, ^c Mean calibration curve uncertainty of the Full Dataset ± Mean Absolute Deviation over the associated calibration period, ^d p value of two-sample Students t-tests assuming unequal variance, ^e H₁ - The difference between the two populations is statistically significant at p = 0.05, H₀ - The difference between the two populations is not statistically significant at p = 0.05

Table 3

Name	UTM Coordinates ^a		Elevation (m)	Mean R-Value	SEM ^b
Maladeta Calibration Boulder	307424	4727841	1906	52.60	0.74
Bassies Calibration Boulder	374343	4733594	853	44.14	0.60
Carlit Calibration Boulder	422066	4707335	1820	48.67	0.65

^a with reference to WGS 1984 31 T, ^b Standard Error of the Mean

Site	Sample ID	Latitude (°)	Longitude (°)	Elevation (m)	Mean R-Value	MAD ^a	SEM ^b	Age (ka)	1 σ
A	CGI-01	42.607017	1.952433	2238	57.84	3.53	0.80	7.93	1.72
	CGI-02	42.606861	1.95218	2235	55.77	4.51	1.05	9.53	1.71
	CGI-03	42.606823	1.951876	2226	57.14	5.73	1.28	8.47	1.71
	CGI-04	42.606635	1.952086	2223	58.81	3.83	0.85	7.20	1.72
	CGI-05	42.606501	1.9521	2214	56.48	4.64	1.01	8.98	1.71
	CGI-06	42.606437	1.95204	2213	57.78	4.03	0.93	7.98	1.72
	CGI-07	42.606062	1.952364	2207	57.74	3.22	0.74	8.01	1.72
	CGI-08	42.605765	1.952466	2208	56.01	4.07	0.90	9.35	1.71
	CGI-09	42.605515	1.952653	2195	55.51	5.00	1.18	9.74	1.71
	CGI-10	42.605363	1.952753	2193	57.88	4.96	1.13	7.90	1.72
	CGI-11	42.605147	1.952745	2186	55.78	5.15	1.21	9.53	1.71
	CGI-12	42.604889	1.953176	2188	55.58	6.50	1.37	9.69	1.71
	CGI-13	42.604872	1.953261	2183	57.38	4.70	1.06	8.29	1.71
	CGI-14	42.604664	1.953143	2184	56.01	4.00	0.90	9.35	1.71
	CGI-15	42.604396	1.953379	2174	54.71	7.03	1.47	10.38	1.71
	CGI-16	42.604096	1.953116	2173	58.41	3.60	0.86	7.50	1.72
	CGI-17	42.604168	1.953066	2168	55.88	5.89	1.32	9.45	1.71
	CGI-18	42.604328	1.952819	2187	57.21	4.73	1.00	8.41	1.71
	CGI-19	42.604096	1.952153	2183	56.45	5.87	1.26	9.01	1.71
	CGI-20	42.604096	1.95208	2184	56.38	4.63	1.04	9.06	1.71
B	CGO-01	42.602443	1.954558	2177	51.35	5.96	1.25	13.18	1.70
	CGO-02	42.602373	1.954717	2176	49.61	4.41	0.98	14.69	1.70
	CGO-03	42.602373	1.954717	2176	51.08	4.47	0.93	13.40	1.70
	CGO-04	42.602401	1.95479	2167	50.21	5.09	1.10	14.16	1.70
	CGO-05	42.602401	1.95479	2167	50.21	5.11	1.16	14.16	1.70
	CGO-06	42.602348	1.954937	2170	52.25	5.32	1.16	12.41	1.70
	CGO-07	42.602213	1.955013	2162	52.41	6.07	1.29	12.27	1.70
	CGO-08	42.602215	1.955208	2169	49.38	5.06	1.06	14.89	1.70
	CGO-09	42.602287	1.955194	2163	49.61	4.33	0.93	14.69	1.70
	CGO-10	42.602307	1.955389	2166	51.61	6.48	1.45	12.95	1.70
	CGO-11	42.602263	1.95556	2171	50.08	4.61	1.03	14.27	1.70
	CGO-12	42.602291	1.955645	2164	52.95	4.53	0.95	11.82	1.70
	CGO-13	42.602382	1.955766	2165	51.61	6.51	1.35	12.95	1.70
	CGO-14	42.602436	1.955728	2165	51.98	5.57	1.22	12.63	1.70
	CGO-15	42.602472	1.955691	2165	51.91	5.58	1.29	12.69	1.70
	CGO-16	42.602545	1.955799	2167	49.88	5.39	1.14	14.45	1.70
	CGO-17	42.602589	1.955701	2167	49.98	4.24	0.98	14.36	1.70
	CGO-18	42.602705	1.955553	2166	52.48	4.40	1.08	12.21	1.70
	CGO-19	42.602749	1.955442	2169	52.15	7.06	1.49	12.49	1.70
	CGO-20	42.602785	1.955442	2169	50.05	3.51	0.86	14.30	1.70
	LDB-01	42.582627	1.99748	2046	45.95	3.62	0.94	18.06	1.69
	LDB-02	42.582494	1.997653	2046	47.58	5.54	1.24	16.53	1.69
	LDB-03	42.582358	1.997582	2047	47.55	4.56	0.99	16.56	1.69
	LDB-04	42.582286	1.99751	2046	48.65	4.57	0.98	15.55	1.69

C	LDB-05	42.582141	1.997464	2048	48.58	4.46	1.02	15.61	1.69	
	LDB-06	42.582015	1.997466	2051	47.58	4.77	1.07	16.53	1.69	
	LDB-07	42.581978	1.997381	2052	48.35	4.80	1.05	15.82	1.69	
	LDB-08	42.581968	1.997198	2054	48.08	3.60	0.80	16.06	1.69	
	LDB-09	42.58193	1.997028	2055	48.08	5.34	1.14	16.06	1.69	
	LDB-10	42.581829	1.996847	2056	48.18	4.32	0.98	15.97	1.69	
	LDB-11	42.581853	1.996493	2059	48.42	4.04	0.91	15.76	1.69	
	LDB-12	42.581869	1.996274	2058	49.08	4.53	1.03	15.16	1.69	
	LDB-13	42.58174	1.995935	2058	47.98	4.63	1.02	16.16	1.69	
	LDB-14	42.581766	1.995763	2058	47.72	3.95	0.86	16.40	1.69	
	LDB-15	42.581746	1.995557	2052	48.38	5.02	1.13	15.79	1.69	
	LDB-16	42.581773	1.995495	2050	49.05	4.50	0.97	15.19	1.69	
	LDB-17	42.581736	1.995423	2051	48.02	5.40	1.23	16.12	1.69	
	LDB-18	42.581762	1.995288	2048	48.02	5.87	1.21	16.12	1.69	
	LDB-19	42.581644	1.995181	2048	49.89	4.93	1.08	14.44	1.70	
	LDB-20	42.581687	1.995034	2048	49.35	4.62	1.05	14.92	1.70	
	D	MLI01	42.509716	2.101574	1703	40.25	7.37	1.61	23.89	1.70
		MLI02	42.509871	2.101743	1699	39.89	4.34	0.99	24.29	1.70
		MLI03	42.509926	2.101936	1699	38.79	4.32	0.99	25.52	1.71
		MLI04	42.510077	2.102738	1699	40.69	4.07	0.92	23.42	1.70
MLI05		42.509967	2.103713	1688	40.96	5.61	1.23	23.13	1.70	
MLI06		42.510328	2.103854	1687	40.02	5.34	1.21	24.14	1.70	
MLI07		42.51022	2.104963	1685	39.72	3.61	0.84	24.47	1.70	
MLI08		42.510503	2.10541	1683	39.82	4.51	1.05	24.36	1.70	
MLI09		42.510651	2.105894	1686	39.12	5.19	1.22	25.14	1.70	
MLI10		42.510681	2.10632	1685	38.79	3.50	0.81	25.52	1.71	
MLI11		42.510836	2.106512	1683	39.36	5.54	1.23	24.88	1.70	
MLI12		42.510873	2.106695	1684	38.39	4.22	0.89	25.98	1.71	
MLI13		42.511027	2.106826	1684	38.15	4.74	1.05	26.25	1.71	
MLI14		42.511128	2.107032	1684	40.46	4.19	1.02	23.67	1.70	
MLI15		42.511346	2.107309	1684	41.06	5.77	1.30	23.02	1.70	
MLI16		42.511528	2.107489	1683	39.26	5.24	1.16	24.99	1.70	
MLI17		42.511747	2.107887	1680	41.32	5.57	1.17	22.73	1.70	
MLI18		42.512164	2.108246	1679	39.26	4.52	1.00	24.99	1.70	
MLI19		42.512435	2.10834	1679	39.36	4.36	1.02	24.88	1.70	
MLI20		42.512498	2.108339	1679	38.96	5.52	1.22	25.33	1.71	
MLO01	42.51083	2.111576	1619	27.38	6.26	1.43	40.85	1.81		
MLO02	42.510621	2.111348	1619	28.35	5.40	1.31	39.32	1.80		
MLO03	42.510485	2.111253	1618	27.48	5.77	1.23	40.69	1.81		
MLO04	42.510306	2.111316	1618	27.98	5.51	1.27	39.89	1.80		
MLO05	42.510251	2.111244	1618	24.78	5.45	1.22	45.24	1.86		
MLO06	42.510224	2.111122	1617	26.88	4.81	1.15	41.66	1.82		
MLO07	42.510215	2.111317	1618	27.65	6.03	1.43	40.42	1.81		
MLO08	42.510006	2.111052	1617	25.48	6.70	1.42	44.01	1.84		
MLO09	42.509898	2.110981	1618	27.68	6.18	1.35	40.37	1.81		

E	MLO10	42.509887	2.110774	1619	27.55	5.30	1.19	40.58	1.81
	MLO11	42.509731	2.110338	1621	28.15	6.02	1.40	39.63	1.80
	MLO12	42.509657	2.110108	1622	26.82	8.22	1.81	41.77	1.82
	MLO13	42.509457	2.109916	1622	28.59	6.10	1.32	38.96	1.79
	MLO14	42.509383	2.109613	1623	26.82	4.86	1.11	41.77	1.82
	MLO15	42.509292	2.109578	1624	27.45	6.13	1.38	40.74	1.81
	MLO16	42.508837	2.108963	1632	28.49	5.03	1.11	39.11	1.79
	MLO17	42.508762	2.108514	1635	27.35	7.29	1.49	40.90	1.81
	MLO18	42.508762	2.108502	1636	28.49	5.90	1.31	39.11	1.79
	MLO19	42.50865	2.108089	1637	25.78	4.39	1.05	43.50	1.84
	MLO20	42.508586	2.107932	1637	27.02	5.07	1.13	41.44	1.82

^a Mean Absolute Deviation, ^b Standard Error of the Mean